

## Strained craters on Ganymede

Robert T. Pappalardo<sup>a,\*</sup>, Geoffrey C. Collins<sup>b</sup>

<sup>a</sup>Laboratory for Atmospheric and Space Physics, University of Colorado, Boulder, CO 80309, USA

<sup>b</sup>Department of Physics and Astronomy, Wheaton College, Norton, MA 02766, USA

Received 12 June 2004; received in revised form 28 October 2004; accepted 10 November 2004

### Abstract

High-resolution images of Jupiter's satellite Ganymede obtained by the Galileo spacecraft reveal several elliptical craters that are transected by sets of subparallel ridges and troughs oriented roughly orthogonal to the long axis of the crater, implying that these craters have been extensionally strained. We analyze five such craters, four in the ancient dark terrain and one in bright grooved terrain, inferring their strain histories by assuming each crater was originally circular. These strained craters have been elongated by amounts ranging from ~5 to ~50%. All are deformed by extension near perpendicular to subparallel ridges and troughs, and some are also deformed by distributed simple shear parallel to these tectonic structures. The rift zones that deform these craters show extensions of ~5 up to ~180% for a well-defined fault zone that rifts Saltu crater within dark terrain of Nicholson Regio. Extensional fault zones consisting of domino-style normal faults and representing strains of several tens of percent may be common on Ganymede, and strains of this order can alter pre-existing surface features beyond recognition through the process of tectonic resurfacing.

© 2005 Elsevier Ltd. All rights reserved.

*Keywords:* Ganymede; Craters; Extension; Strain

### 1. Background

#### 1.1. Tectonism on Ganymede

In 1979, moderate resolution Voyager spacecraft images (up to ~500 m/pixel) of Jupiter's ice-rich moon Ganymede revealed bright lineated swaths tens of kilometers wide and up to hundreds of kilometers long, termed 'grooved terrain,' which cross-cut the satellite's ancient dark terrain (Fig. 1a) (Smith et al., 1979a,b). Bright swaths of grooved terrain contain sets of subparallel curvilinear ridges and troughs of regular spacing, commonly trending subparallel to and confined within prominent bounding grooves (Shoemaker et al., 1982; McKinnon and Parmentier, 1986). Based on Voyager regional-scale observations, bright grooved terrain was generally interpreted as having formed by a three-step process: (1) formation of a broad fault-bounded graben in dark terrain; (2) volcanic eruption of relatively clean water and/or ice to flood the broad graben and to resurface the dark

terrain within, creating bright smooth terrain; and (3) further extension to produce the grooved terrain as sets of narrow subparallel graben (Golombek and Allison, 1981; Parmentier et al., 1982; Shoemaker et al., 1982; McKinnon and Parmentier, 1986; Allison and Clifford, 1987).

The assumption that individual grooves represent graben led to estimations of a few percent extensional strain across grooved terrain swaths (Golombek, 1982). This estimate seemed consistent with a ~1% limit on the global expansion of Ganymede imposed by the large-scale coherence of the ancient dark terrain comprising Galileo Regio (McKinnon, 1981), and with the suggestion that grooved terrain extension may be related to global expansion resulting from differentiation of the satellite (Squyres, 1980). It was proposed that strike-slip tectonism might have helped to shape bright grooved terrain (Lucchitta, 1980; Murchie and Head, 1988), but its relative role was unclear because of image resolution limitations.

In 1996, the first high-resolution images returned from the Galileo spacecraft (~75 m/pixel) confirmed that extensional tectonism, along with a component of horizontal simple shear, has been instrumental in shaping grooved terrain in the Uruk Sulcus region (Pappalardo et al., 1998). Stereo imaging of the region subsequently indicated that

\* Corresponding author. Tel.: +1 303 492 6423; fax: +1 303 492 6946  
E-mail address: robert.pappalardo@colorado.edu (R.T. Pappalardo).

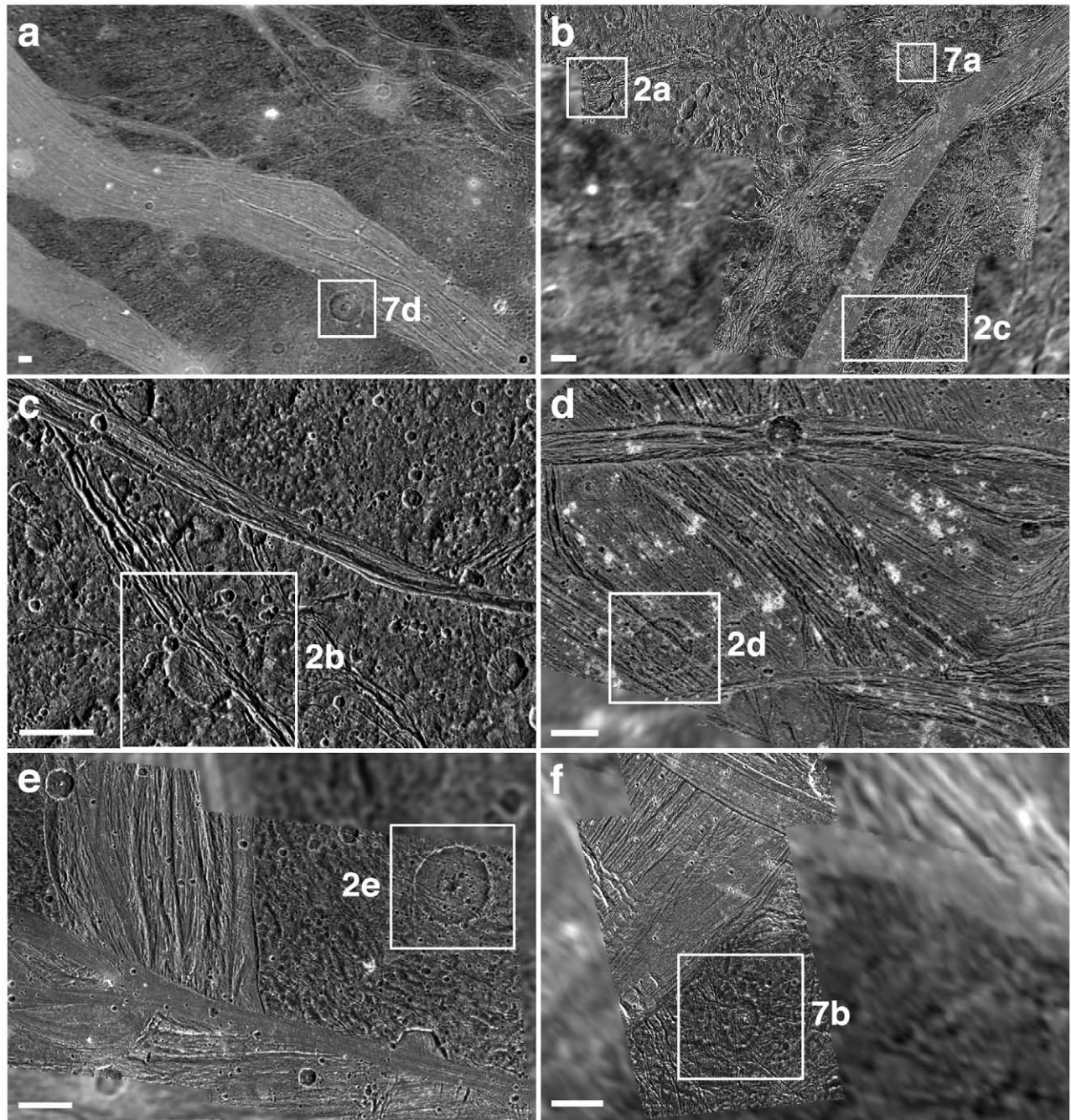


Fig. 1. Regional-scale views of Ganymede, with boxed areas indicating the locations of subsequent figures, as labeled. In each image, the scale bar is 20 km and north is toward the top. (a) Voyager 2 (1 km/pixel) view of dark terrain of Marius Regio, cross-cut by bright grooved terrain of NW-trending Mashu Sulcus. (b) Dark terrain of Nicholson Regio, transected by several fracture sets and by NE-trending Arbela Sulcus (Galileo observations G7GSNICHOL01, 176 m/pixel, and 28GSARBELA02, 133 m/pixel, on Voyager 1 context). (c) Dark terrain of Marius Regio, in the vicinity of WNW-trending Anshar Sulcus (Galileo observation G8GSANSHAR01, 150 m/pixel). (d) Bright grooved terrain of Nun Sulci (Galileo observation G7GSNUNSUL01, 164 m/pixel, on Voyager 1 context). (e) Marius Regio where it borders grooved terrain of N-trending Erech Sulcus and NW-trending Sippar Sulcus (Galileo observation G8GSERECH, 143 m/pixel, on Voyager 2 context). (f) Dark terrain of Marius Regio along its border with NE-trending Philus Sulcus (Galileo observation G2NIPPUR01, 99 m/pixel, overlain onto Galileo image G8GSREGCON01, 920 m/pixel).

fault blocks typically  $\sim 1$  km in topographic wavelength are superimposed on the longer wavelength topography (typically  $\sim 8$  km) that had been imaged by Voyager (Collins et al., 1998a; Pappalardo et al., 1998). The morphologies and geological associations of these fault blocks suggest that

they were formed by domino-style (imbricate) normal faulting (Pappalardo et al., 1998), implying a high degree of extensional strain relative to graben formation (Wernicke and Burchfiel, 1982). A minimum extensional strain of  $\sim 50\%$  was estimated by Collins et al. (1998a) based on the

geometry of fault blocks as inferred from these high-resolution Uruk Sulcus images. However, it remained unclear whether such high extensional strain was representative of grooved terrain or relatively rare.

Galileo images obtained during subsequent encounters with Ganymede showed that zones of subparallel ridges and troughs also exist within the ancient dark terrain (e.g. Fig. 1b) (Patel et al., 1999; Prockter et al., 2000). Unlike most areas within the grooved terrain, lanes of ridge and trough terrain within dark terrain do not occur in well-defined sets confined by prominent bounding grooves. We adopt the generic term ‘ridge and trough terrain’ (RTT) (Pappalardo and Greeley, 1995) as inclusive of ridge-and-trough sets of various specific morphologies within both bright and dark terrains on Ganymede. The morphologies of dark terrain RTT are analogous to those in some bright grooved terrain, and the structures have been similarly interpreted as domino-style normal fault blocks (Patel et al., 1999). This interpretation implies that high-strain normal faulting may have occurred within dark terrain regions as well.

### 1.2. Tectonic resurfacing hypothesis

Based on analysis of the Uruk Sulcus region, Head et al. (1997a) suggested that high-strain domino-style normal faulting might be able to deform pre-existing topography to the extent that it is unrecognizable, effectively ‘tectonically resurfacing’ older terrains without the aid of icy volcanism. Expanding on this model, Patel et al. (1999) suggested that in pervasively faulted RTT zones within dark terrain, a thin veneer of dark material may shed into topographic lows to reveal underlying brighter, icier material along upfaulted ridge crests and slopes, resulting in a greater integrated brightness of faulted terrain in regions lacking any icy volcanism. Subsequently, Schenk et al. (2001) used stereo data to demonstrate that some lanes of bright terrain are low-lying and relatively flat over large distances, consistent with their emplacement through icy volcanism, reinforcing the Voyager-based volcanic resurfacing scenario. Some high-resolution images of Ganymede obtained in May, 2000 show extremely smooth patches within bright terrain, consistent with emplacement through volcanic resurfacing (Giese et al., 2001), and other images show pervasive tectonism, consistent with tectonic resurfacing (Head et al., 2002). The relative roles of tectonism and volcanism in shaping Ganymede’s grooved terrain remains an open issue (Pappalardo et al., 2004).

### 1.3. Craters as strain markers

To test the hypothesis that high-strain imbricate fault blocks are common to RTT on Ganymede and potentially can tectonically resurface pre-existing terrain, we examine tectonically deformed craters, which can serve as strain markers. Craters serve as natural strain markers on tectonically deformed planets because most originate as

near-circular, for all impactors that strike a planetary surface at  $>10^\circ$  from the horizontal (Gault and Wedekind, 1978). Terrestrial structural geologists have a well-established practice of using markers of known initial shape to infer strain (e.g. Ramsay, 1967; Means, 1976; Ramsay and Huber, 1983). Initially spherical objects such as pebbles, oolites, or some fossils are deformed by homogeneous strain ellipsoids. Planar sections through these objects yield elliptical shapes that define the shape and orientation of the strain ellipse in that plane. Determination of angular changes (e.g. through measurements of the angles between initially perpendicular lines of a bilaterally symmetric fossil) in more than one direction can also provide sufficient information to characterize the shape and orientation of the strain ellipse in the measurement plane.

On the planet Mercury, the geometry of deformed craters has been used to infer crustal shortening along presumed reverse faults (Strom et al., 1975; Dzurisin, 1978). The ellipticity of Martian craters has been used to infer the total extensional strain across the craters as well as the strain represented by individual faults (Thomas and Allemand, 1993; Golombek et al., 1996). On Venus, extensional strain across craters has been estimated by assuming that individual lineaments are normal fault scarps that have deformed the craters they transect (Grimm, 1994). All these previous planetary studies only examine the elongation of craters but do not evaluate the relative roles of simple extension and simple shear.

Though few strained craters were recognized in Voyager images of Ganymede (Shoemaker et al., 1982), several strained craters tens of kilometers in size were imaged at relatively high resolution by Galileo. Here, we concentrate on five relatively large strained craters, each elliptical in shape with its long axis approximately orthogonal to the trend of transecting RTT, suggesting that each was extensionally strained during RTT formation. We infer the degree of extensional strain and horizontal simple shear recorded by each crater, to provide insight into these deformation mechanisms. We note that no examples of shortened craters or other large-scale contractional structures have yet been identified on Ganymede (Pappalardo et al., 2004).

## 2. Strained crater analyses

Each of the five strained craters that we have analyzed in detail (Figs. 1–3 and Table 1) retains recognizable rim segments along a substantial portion of its circumference, allowing the pre-deformation crater diameter ( $L_0$ ) and the amount of crater elongation ( $E_C$ ) to be estimated by one of two methods, depending on whether the crater is transected and split by a zone of RTT (Method 1), or if the RTT is distributed across the entire crater (Method 2). Each of these methods can then be used to calculate the displacement by

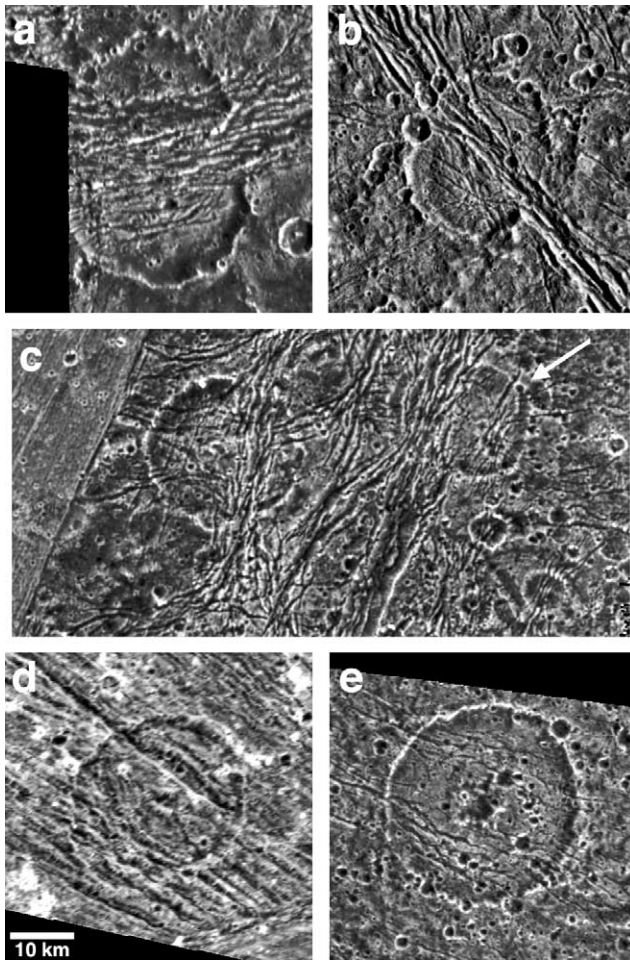


Fig. 2. The extensionally strained craters examined, shown at a common scale. The crater images are in Lambert azimuthal equal area projections, each centered on the target crater. (a) Saltu, within dark terrain of Nicholson Regio. (b) Unnamed crater in dark terrain of Marius Regio, near Anshar Sulcus. (c) A pair of strained craters, east of Arbelia Sulcus; arrow indicates the analyzed crater. (d) Nefertum, within grooved terrain of Nun Sulci. (e) Erichthonius, east of Erech Sulcus.

simple extension ( $d_E$ ) and the displacement by simple shear ( $d_S$ ) accommodated by the RTT. All measurements of crater strain are performed using images in Lambert azimuthal equal area projection centered on the approximate center of the crater, preserving the shapes of concentric features. Although this projection is neither conformal nor equidistant, all measurements are obtained  $<0.5^\circ$  from the map projection center, ensuring negligible measurement error from map distortion.

### 2.1. Method 1: split craters

Method 1 is used where a narrowly constrained zone of RTT transects a crater, leaving two relatively undeformed arc-shaped rim segments on either side of the RTT (e.g. Saltu, Figs. 2a and 3a). Locations along the crest of each of the two intact rim segments were digitized, and best-fit circles were calculated for each of the two sets of points.

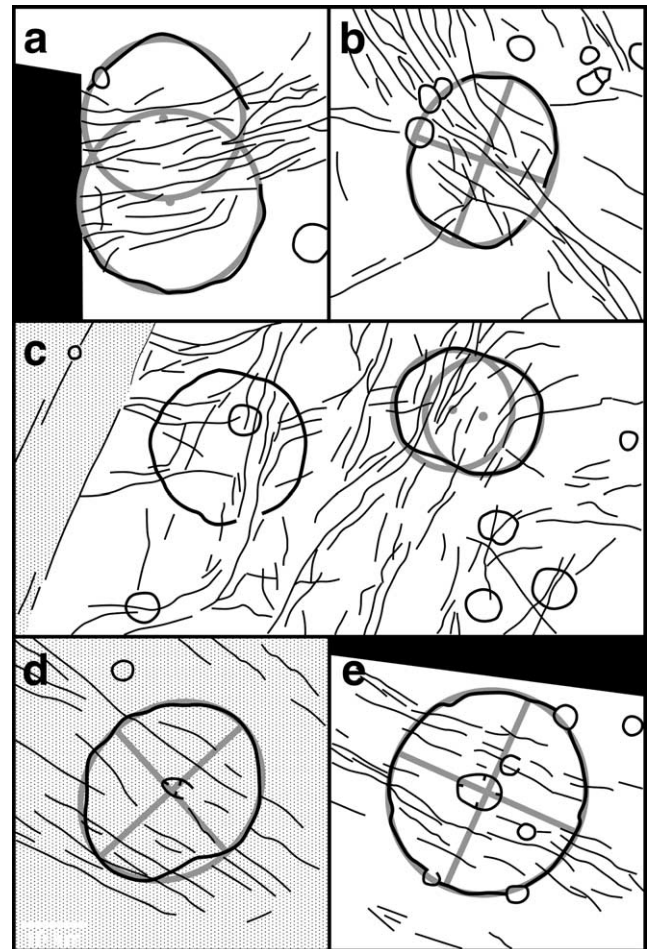


Fig. 3. Sketch maps of strained craters depicted in Fig. 2. For those craters analyzed by Method 1 ((a) and (c)), shown in gray are the circles fit to each rim segment and their corresponding centers. For craters analyzed by Method 2 ((b), (d) and (e)), shown in gray are the best-fit ellipses and their corresponding major and minor axes. Representative troughs and other craters are shown, and stipples indicate areas of bright terrain. The central pits of pit craters are marked by inward-pointing ticks.

The best fit circles were calculated by finding the radius and center coordinates that minimize the RMS error between the equation for a circle and the set of digitized points, using an algorithm for the downhill simplex method (Press et al., 1992). For each crater measured using Method 1, the pre-deformation crater rim diameter  $L_0$  reported in Table 1 is an average of repeated measurements of the best fit circles from the two intact rim segments, and the error is compounded from averaging the best fit circles and their associated RMS errors (e.g. Taylor, 1996). A line is then drawn through the centers of the two best fit circles, and the distance from the outer edge of one circle to the outer edge of the other circle is adopted as the final (strained) crater major axis  $L_1$  (Fig. 4). For comparison with previous studies of strained craters on other planets (Section 1.3), we calculate the crater elongation as

$$E_C = (L_1/L_0) - 1. \quad (1)$$

Table 1  
Characteristics of five extensionally strained craters imaged by Galileo and analyzed in this study

Crater	Saltu	Marius unnamed	Nicholson unnamed	Nefertum	Erichthonius
Figure numbers	1b, 2a	1c, 2b	1b, 2c	1d, 2d	1e, 2e
Galileo observation	G7GSNICHOL01	G8GSANSHAR01	28GSARBELA02	G7GSNUNSUL01	G8GSERECH_01
Resolution (m/pixel)	176	150	130	164	143
Crater geographic location	Nicholson Regio	Marius Regio	Nicholson Regio	Nun Sulci	Marius Regio
Terrain type	Dark	Dark	Dark	Bright	Dark
Center latitude, longitude	14.1S, 352.9W	11.1N, 191.4W	17.7S, 346.4W	44.4N, 321.1W	15.38S, 175.32W
Method used	Method 1	Method 2	Method 1	Method 2	Method 2
Original crater diameter, $L_0$ (km)	$26.2 \pm 2.1$	$23.3 \pm 0.5$	$18.2 \pm 0.5$	$25.7 \pm 0.1$	$30.2 \pm 0.1$
Minor axis length, $L_2$ (km)	–	$22.2 \pm 0.2$	–	$25.6 \pm 0.1$	$30.2 \pm 0.1$
Major axis length, $L_1$ (km)	$39.0 \pm 1.3$	$26.9 \pm 0.2$	$22.9 \pm 0.4$	$29.9 \pm 0.2$	$31.8 \pm 0.1$
Major axis azimuth, $A_M$	N6W	$N19.2E \pm 1.0^\circ$	N77W	$N47.8E \pm 1.5^\circ$	$N24.1E \pm 2.1^\circ$
Crater elongation, $E_C$ (%)	$48.9 \pm 0.1$	$15.3 \pm 0.0$	$25.8 \pm 0.1$	$16.2 \pm 0.0$	$5.2 \pm 0.0$
RTT azimuth, $A_R$	$N80.1E \pm 4.9^\circ$	$N39.0W \pm 8.5^\circ$	$N25.7E \pm 9.2^\circ$	$N55.2W \pm 4.6^\circ$	$N68.1W \pm 8.0^\circ$
Major axis-RTT angle, $\theta$ ( $^\circ$ )	$+86 \pm 5$	$-58.2 \pm 6.2$	$-77 \pm 9$	$+77.0 \pm 3.5$	$+87.8 \pm 5.9$
Simple shear displacement, $d_S$ (km)	$0.9 \pm 1.1$	$-4.5 \pm 0.7$	$-1.1 \pm 0.7$	$2.0 \pm 0.6$	$0.1 \pm 0.4$
Simple extension displacement, $d_E$ (km)	$12.8 \pm 0.9$	$2.5 \pm 1.1$	$4.6 \pm 0.3$	$3.9 \pm 0.3$	$1.5 \pm 0.2$
RTT zone final width, $R_F$ (km)	$20.6 \pm 2.4$	–	$8.8 \pm 0.8$	–	–
RTT zone original width, $R_0$ (km)	$7.0 \pm 2.4$	–	$4.3 \pm 0.9$	–	–
Total RTT extension, $E_{RTT}$ (%)	$183 \pm 68$	$> 10.5 \pm 4.5^a$	$107 \pm 27$	$15.3 \pm 1.3$	$5.1 \pm 0.5$

<sup>a</sup> Minimum estimate because most of the strain appears to be concentrated in a narrow zone (see text).

The total displacement across the RTT zone is represented by a vector connecting the two circle centers. The magnitude  $d$  of this vector is related to the measured crater diameter and major axis by

$$d = L_1 - L_0. \quad (2)$$

This displacement vector may be a combination of simple extension and simple shear components across the faults of the RTT zone. The displacement caused by simple extension is the component of the displacement vector perpendicular to the faults in the RTT zone

$$d_E = d \sin \theta, \quad (3)$$

while the displacement due to simple shear is the component of the displacement vector parallel to the faults in the RTT zone

$$d_S = d \cos \theta. \quad (4)$$

The angle  $\theta$  is measured between the average azimuth  $A_R$  of faults in the RTT zone and the azimuth  $A_M$  of the displacement vector; clockwise is defined as positive  $\theta$ .

The intact rim segments on either side of the RTT zone serve as relatively undeformed markers for the deformation

within the RTT zone. The observed width of the RTT zone varies within each of the craters, and the average measured value is labeled  $R_F$  in Table 1. The original width of the RTT zone,  $R_0$ , is found by subtracting the amount of simple extension  $d_E$  from  $R_F$ . The extensional strain across the RTT zone is then

$$E_{RTT} = (R_F/R_0) - 1. \quad (5)$$

Table 1 includes error estimates. For  $L_0$ , errors are based on best-fit circle approximations to digitized crater segments, again using the downhill simplex method (Press et al., 1992). Errors for  $L_1$  and  $R_F$  are based on the standard deviation of repeated measurements, and errors for  $A_R$  are based on repeated measurements of the RTT trend within the deformed crater and the associated  $1-\sigma$  variation in measured trend. Error estimates for other derived values are based on standard propagation of measurement errors (e.g. Taylor, 1996) as measured parameters are employed in the equations above.

## 2.2. Method 2: distributed deformation

Method 2 is used for craters pervasively deformed by

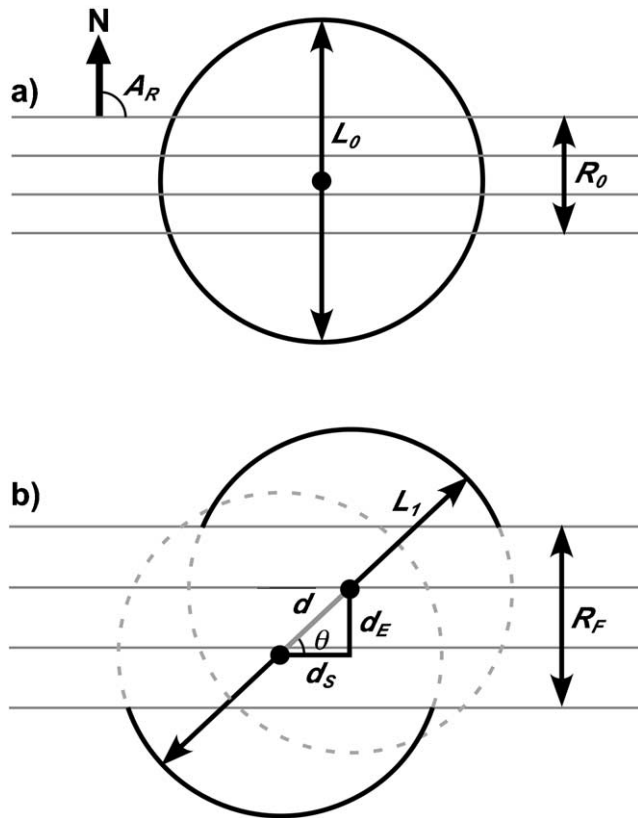


Fig. 4. Parameter definitions for strain measurements by Method 1. The crater rim is represented as a thick black line, while faults are represented by horizontal gray lines. (a) Before strain:  $L_0$  is the original crater diameter,  $R_0$  is the pre-extension width of the RTT zone,  $A_R$  is the azimuth of the RTT zone. (b) After strain:  $L_1$  is the crater rim-to-rim distance along a line passing through the best fit circle centers,  $d$  is the displacement vector,  $d_E$  is the simple extension component of the displacement vector,  $d_S$  is the simple shear component of the displacement vector, and  $R_F$  is the observed width of the RTT zone.

distributed RTT, notably Nefertum (Figs. 2d and 3d) and Erichthonius (Figs. 2e and 3e). In such distributed deformation, the deformed crater rim closely approximates a strain ellipse (Fig. 5). The pre-deformation crater rim diameter  $L_0$  is preserved along a line parallel to the RTT trend, whether the faults in the RTT have accommodated extension and/or simple shear of the crater. To determine the strain that has affected each crater, locations were digitized along the deformed rim, and a best-fit ellipse was calculated by finding the center coordinates, major axis  $L_1$ , minor axis  $L_2$ , and major axis azimuth  $A_M$  that minimize the RMS error between the equation for an ellipse and the set of digitized points, using the downhill simplex method (Press et al., 1992). Measurement errors were determined by the RMS error of this minimization method, repeating this process with 20 different complete sets of digitized rim segments and then calculating a final standard deviation based on the repeated measurements, each with its own associated error.

With the shape and orientation of the strain ellipse

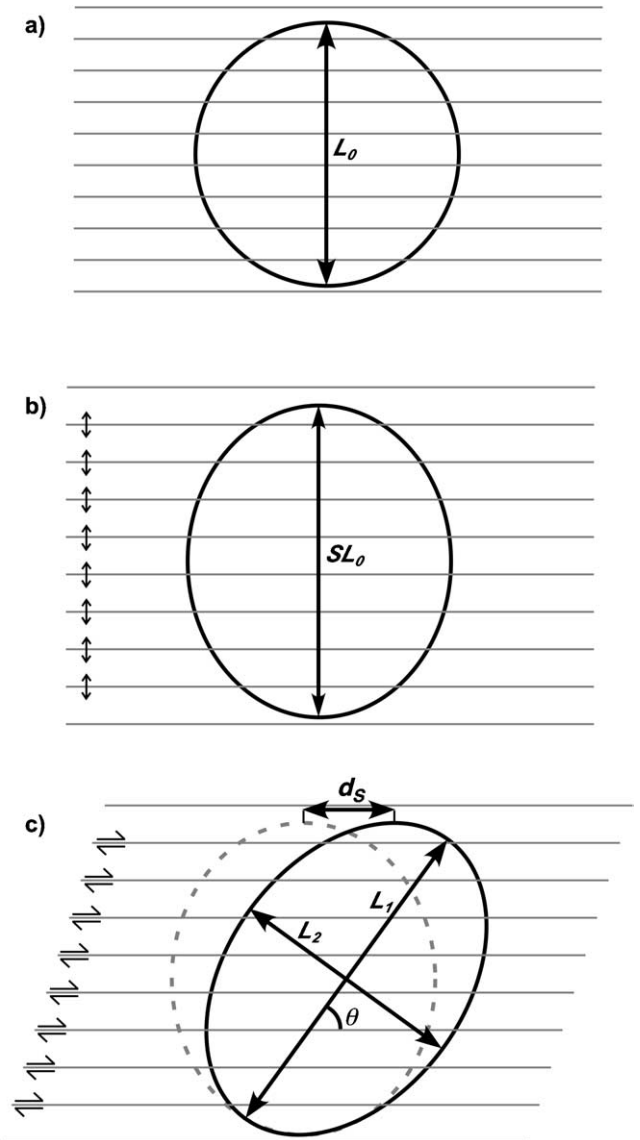


Fig. 5. Parameter definitions for strain measurements by Method 2. (a) Before strain:  $L_0$  is the original crater diameter. (b) After simple extension only:  $S$  is the stretch of the axis of the crater perpendicular to the faults. (c) After simple extension and simple shear:  $L_1$  is the major axis of the ellipse,  $L_2$  is the minor axis of the ellipse,  $\theta$  is the angle between the RTT and the major axis,  $d_S$  is the displacement by simple shear of the top of the crater relative to the bottom, and the dashed gray line represents the pre-shear ellipse from (b). Although a sequence of simple extension followed by simple shear is shown for clarity of explanation, the sequence of shear vs. extension cannot be determined.

determined, the amount of simple extension and simple shear accommodated by the RTT can be found. The ratio of the major axis to the minor axis of the ellipse  $L_1/L_2$  is the ellipticity  $R$ , and the angle between the RTT trend and the major axis of the ellipse is  $\theta$ . Following the reasoning of Ramsay (1967), we derive the equations for a strain ellipse that includes both the shear strain  $\gamma$  and the stretch  $S$  due to simple extension. The quadratic elongations of the strain ellipse are related to the stretch and shear strain as

$$\lambda_1, \lambda_2 = \frac{1}{2} \left( 1 + S^2 + \gamma^2 \pm \sqrt{S^4 + 2S^2(\gamma^2 - 1) + (\gamma^2 + 1)^2} \right). \quad (6)$$

The ellipticity may be written in terms of the quadratic elongations as

$$R^2 = \lambda_1/\lambda_2, \quad (7)$$

and the angle  $\theta$  between the RTT and the major axis of the ellipse is related as

$$\tan \theta = \gamma \left( \frac{\gamma^2}{S} + \frac{1}{S} - \frac{S}{\lambda_1} \right)^{-1}. \quad (8)$$

The results of these equations are plotted in Fig. 6, which shows that for each value of  $R$  and  $\theta$ , the values of  $S$  and  $\gamma$  are uniquely constrained. Note that there is no way to distinguish between (1) extension followed by horizontal shearing, (2) horizontal shearing followed by extension, or (3) simultaneous horizontal shearing and extension; the final strain ellipse will be the same regardless of the sequence of deformation.

For each crater measured using Method 2, we use the values of  $L_1$ ,  $L_2$ , and  $A_M$  from the best fit ellipse, together with the measured azimuth  $A_R$  of the RTT to calculate  $R$  and  $\theta$ . We then use Eqs. (6)–(8) to determine the stretch and shear strain consistent with the currently observed crater shape. Because of the complexity of Eqs. (5) and (7), it is difficult to mathematically propagate the errors in  $R$  and  $\theta$  to errors in  $S$  and  $\gamma$ ; therefore, we estimated these errors by plotting the contours of the error ranges in  $R$  and  $\theta$  on a plot of  $S$  vs.  $\gamma$ .

The displacement by simple extension  $d_E$  is then simply

$$d_E = L_0(S - 1), \quad (9)$$

from the definition of stretch, while the displacement by simple shear  $d_S$  is the product of the shear strain  $\gamma$  and the length  $L_0 S$  of the strain ellipse perpendicular to the RTT direction

$$d_S = L_0 S \gamma \quad (10)$$

as illustrated by Fig. 5. Values of  $d_S$  are reported in Table 1 with positive defined as dextral shear, and negative as sinistral. The extensional strain across the RTT is simply

$$E_{RTT} = S - 1. \quad (11)$$

Errors in  $d_E$ ,  $d_S$ , and  $E_{RTT}$  were propagated from errors in  $L_0$ ,  $S$ , and  $\gamma$  based on standard techniques (e.g. Taylor, 1996). Because the RTT is distributed throughout the crater, we do not report values for the initial and final widths of the RTT zone for craters measured by Method 2.

### 3. Results

The characteristics of the strained craters are summarized in Table 1 along with the results of the strain analyses.

#### 3.1. Saltu

Saltu crater (provisionally named by the International Astronomical Union) is located within the dark terrain of Nicholson Regio (Figs. 2a and 3a). Voyager images of this region revealed curvilinear structures resembling furrows, in close association with ‘dark smooth material’, which was proposed to be cryovolcanic in origin (Murchie et al., 1989). Galileo images (Fig. 1b) reveal no evidence for icy volcanism in the area; instead, brighter patches are associated with fracture zones and commonly appear to be higher in elevation, with darker material shedding into topographic lows (Moore et al., 1999; Prockter et al., 2000). Furthermore, the apparent furrows are instead well-defined zones of RTT.

One such RTT zone cuts the crater Saltu. Bright lineaments are generally inferred to be high-standing ridges and steep slopes, while dark lineaments are low-lying troughs, analogous to those observed elsewhere on Ganymede (Pappalardo et al., 1998; Oberst et al., 1999; Prockter et al., 2000). Fourier analysis shows that multiple topographic wavelengths exist here, similar to those found in bright grooved terrain (Patel et al., 1999); thus, this RTT may have formed by normal faulting and extensional necking of the lithosphere, analogous to formation of bright grooved terrain (Collins et al., 1998a; Dombard and McKinnon, 2001). The lack of identifiable cryovolcanic materials here implies that formation of at least some RTT on Ganymede does not require icy volcanism.

Using Method 1 described above, we find Saltu has lengthened by 49% in a NNW–SSE direction. The displacement due to dextral simple shear is  $0.9 \pm 1.1$  km, so shear in this area is minor, and not required to explain the characteristics of Saltu. The extensional strain across the RTT zone alone is nominally 180%, the highest local strain yet inferred on Ganymede.

#### 3.2. Marius Regio unnamed

Unnamed crater B (Figs. 2b and 3b) is located within Marius Regio, ~30 km south of the southeastern tip of Anshar Sulcus. Prockter et al. (2000) have mapped the structures in this region as identified in Galileo images (Fig. 1c), finding evidence for a two-stage stress history. The first stage involved formation of the rift zone that cuts the unnamed crater B, while the second stage involved a ~25° counterclockwise rotation of the stress field and included transtensional rifting to form Anshar Sulcus.

Measurement using Method 2 shows that the Marius unnamed crater has been elongated by 15% overall. Analysis of this crater is complicated because it is crosscut by two RTT sets. The more subdued set, inferred to be the older, is unlikely to accommodate more than a few percent of the extension, based on morphological comparison to the subdued, widely spaced fractures in the Erichthonius crater

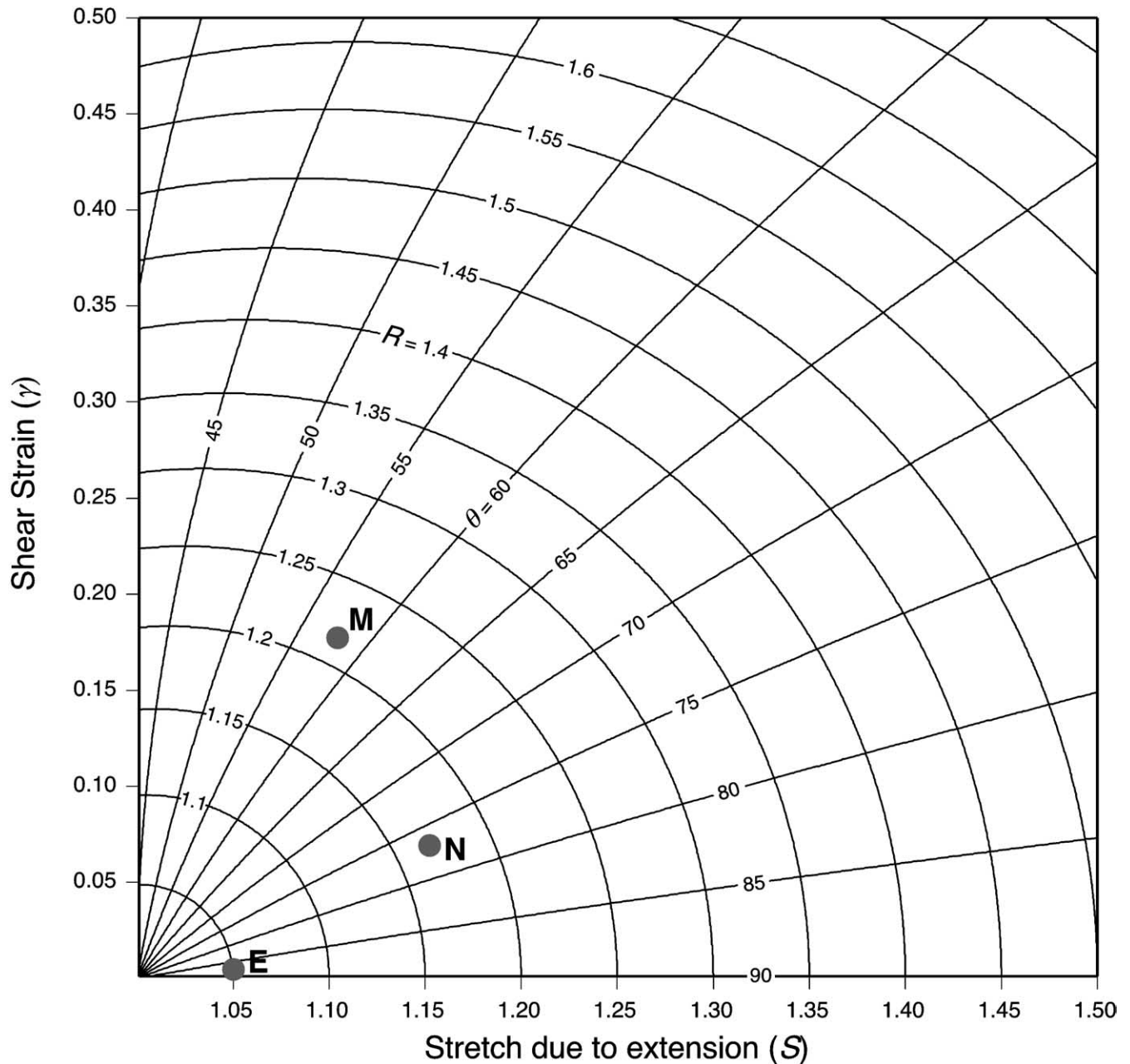


Fig. 6. Plot of shear strain  $\gamma$  vs. stretch  $S$  for Method 2, showing contours of ellipticity  $R$  and angle  $\theta$  between the ellipse's major axis and the RTT faults. Dark circles show the nominal values for craters analyzed using Method 2: Marius unnamed (M), Nefertum (N), and Erichthonius (E).

where low strain is measured (see below). Most of the strain here appears to be accommodated by a narrow RTT zone transecting the crater, but our efforts to apply Method 1 produces results with unrealistically high errors. We infer that Method 1 is confounded by the older fracture sets, which may have already deformed the visible rims into noncircular shapes before the narrow RTT zone deformed the crater. Therefore, we adopt Method 2 for this crater, as this method analyzes the final ellipse produced by the various strains experienced by the crater. For the purposes of measuring the RTT azimuth, we do assume that the prominent RTT zone in the center of the crater accommodated most of the strain.

This crater has the highest measured value of  $\theta$ , indicating that it has accommodated a significant amount of sinistral shear, with a shear displacement across the crater of  $-4.5 \pm 0.7$  km. The  $\approx 10\%$  RTT extensional strain measured by Method 2 is moderate, but if most of this extension is accommodated in the narrow ( $R_F = 7.2 \pm 2.0$  km) RTT zone, then the RTT strain in this zone could be over 50%.

The inferred sense of shear for both sets of RTT structures is opposite to the dextral shear sense implied by Anshar Sulcus itself, but this may be consistent with the obliquely oriented RTT acting as antithetic shears. The

orientation of the more prominent (newer) RTT structures is a good match to the expected orientation of sinistral shears that formed antithetic to Anshar Sulcus itself (see fig. 8b in Prockter et al., 2000). The degraded (older) RTT structures are a much better match to the expected orientation of dextral antithetic structures in the epoch preceding the inferred regional stress rotation.

### 3.3. Nicholson Regio unnamed

The unnamed crater in question within Nicholson Regio (Fig. 2c, arrow, and Fig. 3c) is located 53 km east of Arbela Sulcus (Fig. 1b), observed at 130 m/pixel during the Galileo G28 encounter with Ganymede. Arbela Sulcus resembles crustal spreading bands on Europa (Prockter et al., 2002), and may have accommodated both extension and left lateral shear, based on reconstruction of older features on either side of the sulcus (Head et al., 2002).

The Nicholson Regio unnamed crater is cut by NNE-trending RTT, with most of the faults concentrated in a narrow band in the western portion of the crater. Applying Method 1, elongation of this crater is estimated as 26%. If this extension is all concentrated in the RTT that cuts the western portion of the crater, the extensional strain across this narrow RTT zone is about 100%. Minor sinistral shear ( $d_s = 1.1 \pm 0.7$  km) along the RTT faults is consistent with the dextral sense of shear inferred along Arbela Sulcus, and may form a conjugate set with ENE-trending faults such as those cutting Saltu to the northwest.

### 3.4. Nefertum

Nefertum crater (Figs. 2d and 3d) is located within the Nun Sulci. Interpretations of Voyager images suggested that the region's grooved terrain had undergone sinistral offset, and that this crater might record contraction and shear strain (Murchie and Head, 1988). Analysis of Galileo images (Fig. 1d) supports the interpretation of sinistral horizontal shear along narrow E–W-trending zones that transect the imaged region, but Nefertum is instead found to be strained by NW-trending faults that predate the throughgoing shear zones (Collins et al., 1998b).

Pervasive distributed deformation of Nefertum by RTT of Nun Sulci requires application of Method 2. We estimate that Nefertum is elongated (primarily through extension) by about 16% overall. It is the crater's southwestern rim, where extensional strain is most concentrated, that is deformed nearly beyond recognition. The dextral shear ( $d_s = 2.0 \pm 0.6$  km) could be consistent with late-stage E–W extensional strain inferred in this area (Collins et al., 1998b) being accommodated by shear along these NW-trending faults.

### 3.5. Erichthonius

Erichthonius (Figs. 2e and 3e) lies in the dark terrain of southern Marius Regio, 86 km northeast of the junction of

Erech Sulcus and Sippar Sulcus (Fig. 1e). Erichthonius is the least deformed crater analyzed, estimated by Method 2 to have been elongated through extension by 5%. The troughs cutting Erichthonius are narrow and widely spaced, unlike the RTT in more highly strained craters. Horizontal shear, if any, is inferred to be minor ( $d_s = 0.1 \pm 0.4$  km), and the measurement error makes the sense of shear ambiguous. The morphological characteristics of the troughs transecting Erichthonius and the relatively low extensional strain they accommodate are consistent with these troughs being graben.

## 4. Other strained craters

Some deformed craters observed in Galileo images have experienced multiple generations of extensional deformation and/or shear deformation. For example, Figs. 7a and 8a illustrate an unnamed crater in Nicholson Regio crosscut by fault sets of at least four different orientations. This crater is barely recognizable by the remnants of a bright near-circular rim. Stereo-derived topography of this area confirms a distinct circular depression within this rim (B. Giese, personal communication). This crater has experienced severe tectonism, which could be a principal reason why the crater is barely recognizable in images.

In another example of a severely deformed structure, an elliptical crater (19.9 × 12.2 km) is observed in the dark terrain of Marius Regio, just southeast of the boundary with Philus Sulcus (Figs. 1f, 7b, and 8b) (Head et al., 1997b). At least three differently oriented sets of fractures cut this crater, none of which is aligned with the long or short axes of the crater. The dearth of structures perpendicular to the long axis suggests that this crater was not primarily deformed by extensional strain. Structural relationships in neighboring Philus Sulcus strongly suggest dextral shear in this area (Head et al., 1997b). A distributed network of faint lineaments subparallel to Philus Sulcus cut through this crater, oblique to the crater's long axis. If these lineaments have deformed the crater by simple shear, then the dextral shear inferred within Philus Sulcus also deformed the neighboring dark terrain, including this elliptical crater.

Many smaller strained craters are also found (e.g. Figs. 7c and 8c). However, craters on the order of 10 km or smaller are too small for their strain to be successfully measured by the methods presented above. This is because small alcoves and promontories along the crater rims become large enough with respect to the crater diameter to cause large errors in the circle and ellipse fitting algorithms, precluding measurement of small to moderate strain across these craters.

We note that the 56 km central pit crater Lugalmeslam (Figs. 7d and 8d), on the boundary between the dark terrain of Marius Regio and bright terrain of Mashu Sulcus (Fig. 1a), was targeted by Galileo high resolution imaging in part because it seemed that post-crater activity in grooved terrain might have extended the crater. Moreover, Voyager images suggested that

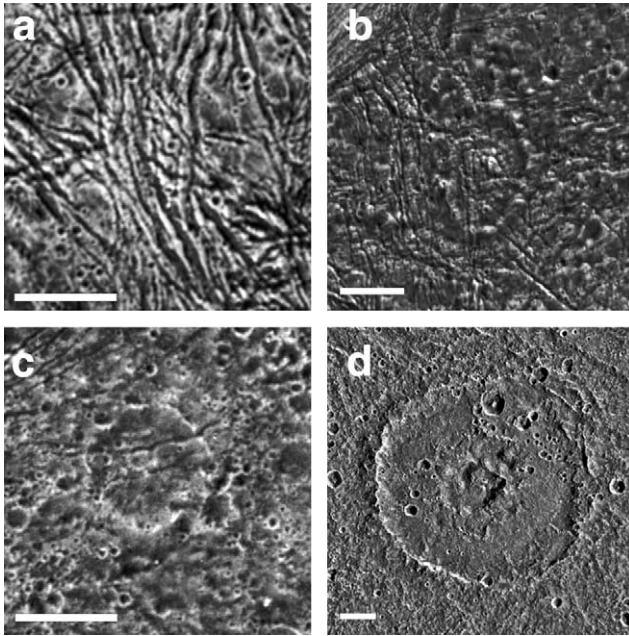


Fig. 7. Additional candidate strained craters, arranged from greatest to least inferred strain. In each image, the scale bar is 10 km and north is toward the top. Lambert azimuthal equal area projections are centered on each crater. (a) A severely deformed crater in Nicholson Regio is recognizable only by fragments of its bright rim crest and by stereo-derived topography (28GSARBELA02, 133 m/pixel). (b) An elliptical crater in Marius Regio near the border of Philus Sulcus may owe its shape to distributed dextral shear (G2NIPPUR01, 99 m/pixel). (c) A crater in Nicholson Regio is transected by narrow tectonic troughs (28GSNICHOL02, 125 m/pixel). (d) The central pit crater Lugalmeslam post-dates both Marius Regio to its southwest and Mashu Sulcus to its northeast, and in Galileo images the crater does not show evidence that it was tectonically strained (G8GSPTCRA01, 146 m/pixel).

bright smooth cryovolcanic material might have extruded into Lugalmeslam (Murchie and Head, 1989). The Galileo image (Fig. 7d) shows that the crater has emplaced a blanket of ejecta on top of Mashu Sulcus, so it post-dates grooved terrain activity. Rather than being extensionally strained, Lugalmeslam's northeastern rim appears to have experienced enhanced failure and collapse where it transected faults in Mashu Sulcus. Furthermore, no discernable evidence of icy volcanism is found: the smooth bright material observed in Voyager images is likely impact melt from the Lugalmeslam impact, rather than volcanically emplaced ice.

## 5. Discussion

The strained craters examined here serve as valuable constraints on the nature of the RTT zones that cut them. Those craters transected by RTT consisting of pervasive, closely spaced ridges and troughs (i.e. all craters of Table 1 other than Erichthonius) are extensionally strained by >10%, while individual RTT swaths can represent strains of >100%. These strains imply rift zones that are

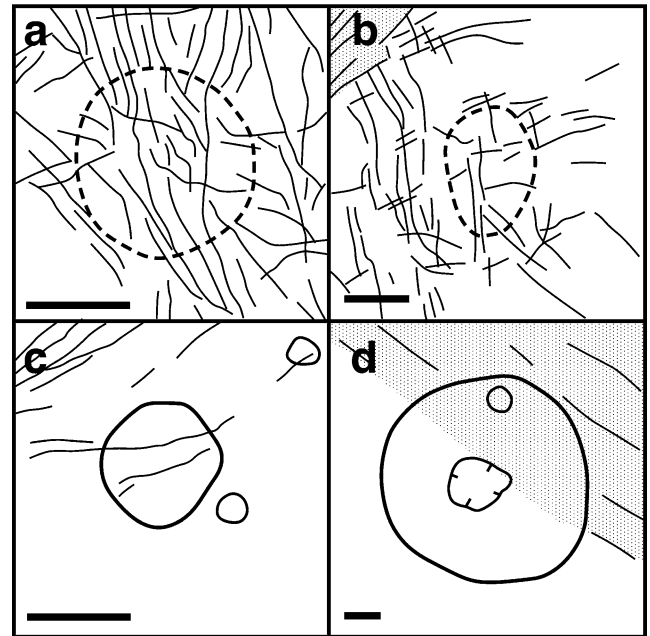


Fig. 8. Sketch maps of craters depicted in Fig. 7. Crater rims are dashed where severely modified. Representative troughs and other craters are shown, and stipples indicate areas of bright terrain. The central pit of Lugalmeslam (d) is marked by inward-pointing ticks.

dominated by domino-style normal faults, rather than sets of narrow graben.

Having measured the relatively low strain portions of deformed craters by Method 1, we infer the highest strains in rift zones that split these craters. These highest strains are in accord with a model of tectonic resurfacing, which at extreme strains may be able to modify pre-existing structures beyond recognition (Head et al., 1997a). The tectonic resurfacing model is supported by two additional observations. First, the craters examined here fall within the size range transitional from central peak to central pit craters on Ganymede (Schenk, 1991). While the least strained craters examined here (Figs. 2d and e, and 7c and d) do retain their central structures, the more highly strained craters (Figs. 2a–c, and 7a) show no obvious central structures, presumably because these structures were tectonically destroyed by RTT formation. Second, the southwestern rim of Nefertum (Fig. 2d), where extensional strain appears to be most concentrated, is deformed nearly beyond recognition, suggesting that this crater (at 15% strain overall) is on the verge of being tectonically destroyed. These observations suggest that ~15% is a lower bound to the amount of strain that may begin to make a crater unrecognizable through tectonic resurfacing, while strains on the order of tens of percent likely can tectonically alter pre-existing structures on Ganymede beyond recognition.

We note that several strained craters were fortuitously captured in Galileo high-resolution images of dark terrain, but only one large strained crater (Nefertum) is observed in

high resolution images of bright terrain. It is feasible that some pre-existing craters in bright terrain have been wiped out by tectonism. This is a plausible scenario if bright grooved terrain has typically experienced tens of percent extension. However, not all bright terrain exhibits high extensional strain, as there are examples of craters in bright terrain that do not exhibit appreciable strain despite being transected by numerous lineaments (Pappalardo et al., 2004).

Highly extended terrains are common in terrestrial environments, where they are balanced by convergence elsewhere. However, large extensional strains seem at odds with the lack of convergence-related structures recognized on Ganymede. Global expansion could have resulted during interior differentiation of the satellite, with corresponding areal expansion of as much as 6.5% (Suyres, 1980; Mueller and McKinnon, 1988). However, the large-scale coherence of dark terrain of Galileo Regio suggests a global expansion limit of  $\sim 1\%$  (McKinnon, 1981). If tilt-block style normal faulting is common on Ganymede, as appears to be the case, then these limits to the total expected extensional strain might be challenged. However, the total amount of extension implied by grooved terrain formation has not yet been evaluated in light of Galileo imaging, as the task is confounded by limited high-resolution coverage. Mapping and morphological classification of ridges and troughs in regional- and global-scale images may enable such an estimate. It may be that Ganymede, like its neighboring satellite Europa (Prockter and Pappalardo, 2000), is hiding at least some degree of contractional strain in low-amplitude, long-wavelength folds, which could be detected by altimetry on a future spacecraft mission.

## 6. Conclusions

Five craters identified in high-resolution images of Jupiter's ice-rich moon Ganymede have been elongated by  $\sim 5\text{--}50\%$ . All are deformed by extension along subparallel ridges and troughs, and some are also deformed by distributed horizontal simple shear along these tectonic structures. Ridge-and-trough fault zones with high extensional strains (tens of percent) may be common on Ganymede and probably consist of domino-style normal faults. Extensional strain  $\sim 15\%$  across Nefertum crater represents a lower bound to the amount of strain that may begin to make a crater unrecognizable, and strains on the order of tens of percent can likely alter pre-existing structures on Ganymede beyond recognition through tectonic resurfacing. A  $\sim 20$  km ridge-and-trough zone that splits Saltu crater has experienced  $\sim 180\%$  extension.

These results for the degree and style of strain represented by crater-deforming tectonic structures will be valuable for application to RTT elsewhere on Ganymede based on morphological comparisons. Deformed craters on Ganymede have experienced some of the greatest tectonic

strains recorded beyond the Earth. Stress mechanisms are unknown but might be related to satellite differentiation, nonsynchronous rotation, or convection (Pappalardo et al., 2004). It is not clear how Ganymede's extensional strain is resolved elsewhere on the satellite because contractional structures are not apparent. The methods for analyzing extensional and shear components of crater strain that are described here can be applied to strained craters on other planets. On Ganymede and other planetary bodies, sets of tectonic structures are relatively unaffected by erosion, so their morphologies and origins serve as well-preserved examples of how strain can modify planetary surfaces.

## Acknowledgements

David Ferrill, Alan Morris, Eric Grosfils, and Steve Reynolds provided very thorough and constructive reviews, which greatly improved the foundations of this work. We also thank Elizabeth Turtle for providing the original circle-fitting program used in this study, Amy Barr for assistance in programming the ellipse fitting program, and Moses Milazzo and Nina Dieter for constructing the Galileo Ganymede image mosaics. This work was funded through NASA Jupiter System Data Analysis Program grant NAG5-8046 and NASA Planetary Geology and Geophysics Program grant NAG5-11616.

## References

- Allison, M.L., Clifford, S.M., 1987. Ice-covered water volcanism on Ganymede. *Journal of Geophysical Research* 92, 7865–7876.
- Collins, G.C., Head, J.W., Pappalardo, R.T., 1998a. The role of extensional instability in creating Ganymede grooved terrain: insights from Galileo high-resolution stereo imaging. *Geophysical Research Letters* 25, 233–236.
- Collins, G.C., Head, J.W., Pappalardo, R.T., Galileo SSI Team, 1998b. Geology of the Galileo G7 Nun Sulci target area, Ganymede, Lunar and Planetary Science Conference XXIX, abstract #1755 [CD-ROM]. Lunar and Planetary Institute, Houston.
- Dombard, A.J., McKinnon, W.B., 2001. Formation of grooved terrain on Ganymede: extensional instability mediated by cold, superplastic creep. *Icarus* 154, 321–336.
- Dzurisin, D., 1978. The tectonic and volcanic history of Mercury as inferred from studies of scarps, ridges, troughs, and other lineaments. *Journal of Geophysical Research* 83, 4883–4906.
- Gault, D.E., Wedekind, J.A., 1978. Experimental studies of oblique impact. *Proceedings of the 9th Lunar and Planetary Science Conference*, pp. 3843–3875.
- Giese, B., Wagner, R., Neukum, G., Pappalardo, R., Head, J.W., Galileo Imaging Team, 2001. The topography of bright/dark terrain on Ganymede, Lunar and Planetary Science Conference XXXII, abstract #1751 [CD-ROM]. Lunar and Planetary Institute, Houston.
- Golombek, M.P., 1982. Constraints on the expansion of Ganymede and the thickness of the lithosphere. *Proceedings of the 13th Lunar and Planetary Science Conference. Journal of Geophysical Research* 87, A77–A83.

- Golombek, M.P., Allison, M.L., 1981. Sequential development of grooved terrain and polygons on Ganymede. *Geophysical Research Letters* 8, 1139–1142.
- Golombek, M.P., Tanaka, K.L., Franklin, B.J., 1996. Extension across Tempe Terra, Mars, from measurements of fault scarp widths and deformed craters. *Journal of Geophysical Research* 99, 23163–23171.
- Grimm, R.E., 1994. Recent deformation rates on Venus. *Journal of Geophysical Research* 99, 23163–23171.
- Head, J.W., Pappalardo, R., Collins, G., Greeley, R., Galileo Imaging Team, 1997a. Tectonic resurfacing on Ganymede and its role in the formation of grooved terrain. *Lunar and Planetary Science Conference. XXVIII 1997*; 535–536.
- Head, J.W., Pappalardo, R., Collins, G., Prockter, L., Galileo Imaging Team, 1997b. Nippur Sulcus Region, Ganymede: Nature of high-latitude groove lanes and their relationship to Marius Regio from Galileo SSI data. *Lunar and Planetary Science Conference. XXVIII 1997*; 537–538.
- Head, J.W., Pappalardo, R., Collins, G., Belton, M.J.S., Giese, B., Wagner, R., Breneman, H., Spaun, N., Nixon, B., Neukum, G., Moore, J., 2002. Evidence for Europa-like resurfacing styles on Ganymede. *Geophysical Research Letters* 29 (24), 251.10.1029/2002GL015961
- Lucchitta, B.K., 1980. Grooved terrain on Ganymede. *Icarus* 44, 481–501.
- McKinnon, W.B., 1981. Tectonic deformation of Galileo Regio and limits to the planetary expansion of Ganymede. In: *Proceedings of the Lunar and Planetary Science Conference*, vol. 12B. Pergamon, New York, pp. 1585–1597.
- McKinnon, W.B., Parmentier, E.M., 1986. Ganymede and Callisto. In: Burns, J.A., Matthews, M.S. (Eds.), *Satellites*. University of Arizona Press, Tucson, pp. 718–763.
- Means, W.D., 1976. *Basic Concepts of Continuum Mechanics for Geologists*. Springer, New York. 339pp.
- Moore, J.M., Asphaug, E., Morrison, D., Spencer, J.R., Chapman, C.R., Sullivan, R.J., Chuang, F.C., Klemaszewski, J.E., Greeley, R., Bender, K.C., Geissler, P.E., Helfenstein, P., Pilcher, C.B., 1999. Mass movement and landform degradation on the icy Galilean satellites: results of the Galileo nominal mission. *Icarus* 140, 294–312.
- Mueller, S., McKinnon, W.B., 1988. Three-layered models of Ganymede and Callisto: compositions, structures, and aspects of evolution. *Icarus* 76, 437–464.
- Murchie, S.L., Head, J.W., 1988. Possible breakup of dark terrain on Ganymede by large-scale shear faulting. *Journal of Geophysical Research* 93, 8795–8824.
- Murchie, S.L., Head, J.W., 1989. Geologic map of the Philus Sulcus quadrangle of Ganymede, US Geological Survey Map I-1966, scale, 1:5,000,000.
- Oberst, J., Schreiner, B., Giese, B., Neukum, G., Head, J., Pappalardo, R., Helfenstein, P., 1999. The distribution of bright and dark material on Ganymede in relationship to surface elevation and slopes. *Icarus* 140, 283–293.
- Pappalardo, R.T., Greeley, R., 1995. A review of the origins of subparallel ridges and troughs: Generalized morphological predictions from terrestrial models. *Journal of Geophysical Research* 100, 18,985–19,007.
- Pappalardo, R.T., Head, J.W., Collins, G.C., Kirk, R.L., Neukum, G., Oberst, J., Giese, B., Greeley, R., Chapman, C.R., Helfenstein, P., Moore, J.M., McEwen, A., Tufts, B.R., Senske, D.A., Breneman, H.H., Klaasen, K., 1998. Grooved terrain on Ganymede: first results from Galileo high-resolution imaging. *Icarus* 135, 276–302.
- Pappalardo, R.T., Collins, G.C., Head, J.W., Helfenstein, P., McCord, T., Moore, J.M., Prockter, L.M., Schenk, P.M., Spencer, J., 2004. Geology of Ganymede. In: Bagenal, F., Dowling, T.E., McKinnon, W.B. (Eds.), *Jupiter: The Planet, Satellites and Magnetosphere*. Cambridge University Press, Cambridge, pp. 363–396.
- Parmentier, E.M., Squyres, S.W., Head, J.W., Allison, M.L., 1982. The tectonics of Ganymede. *Nature* 295, 290–293.
- Patel, J.G., Pappalardo, R.T., Head, J.W., Collins, G.C., Hiesinger, H., Sun, J., 1999. Topographic wavelengths of Ganymede groove lanes from Fourier analysis of Galileo images. *Journal of Geophysical Research* 104, 24,057–24,074.
- Press, W.H., Teukolsky, S.A., Vetterling, W.T., Flannery, B.P., 1992. *Numerical Recipes in C: the Art of Scientific Computing*. Cambridge University Press, New York. 1020pp.
- Prockter, L.M., Pappalardo, R.T., 2000. Folds on Europa: implications for crustal cycling and accommodation of extension. *Science* 289, 941–943.
- Prockter, L.M., Head, J.W., Pappalardo, R.T., Senske, D.A., Neukum, G., Wagner, R., Wolf, U., Oberst, J., Giese, B., Moore, J.M., Chapman, C.R., Helfenstein, P., Greeley, R., Breneman, H.H., Belton, M.J.S., 1998. Dark terrain on Ganymede: geological mapping and interpretation of Galileo Regio at high resolution. *Icarus* 135, 317–344.
- Prockter, L.M., Figueredo, P., Pappalardo, R.T., Head, J.W., Collins, G.C., 2000. Geology and mapping of dark terrain on Ganymede and implications for grooved terrain formation. *Journal of Geophysical Research* 105, 22,519–22,540.
- Prockter, L.M., Head III, J.W., Pappalardo, R.T., Patel, J.G., Sullivan, R.J., Clifton, A.E., Giese, B., Wagner, R., Neukum, G., 2002. Morphology of European bands at high resolution: a mid-ocean ridge-type rift mechanism. *Journal of Geophysical Research* 107 (E5), 101029/2000JE001458.
- Ramsay, J.G., 1967. *Folding and Fracturing of Rocks*. McGraw-Hill, New York. 568pp.
- Ramsay, J.G., Huber, M.I., 1983. *The Techniques of Modern Structural Geology*. Vol. 1: Strain Analysis. Academic Press, New York. 307pp.
- Schenk, P.M., 1991. Ganymede and Callisto: complex crater formation and planetary crusts. *Journal of Geophysical Research* 96, 15,635–15,664.
- Schenk, P.M., McKinnon, W.B., Gwynn, D., Moore, J.M., 2001. Flooding of Ganymede's bright terrains by low-viscosity water-ice lavas. *Nature* 410, 57–60.
- Shoemaker, E.M., Lucchitta, B.K., Plescia, J.B., Squyres, S.W., Wilhelms, D.E., 1982. The geology of Ganymede. In: Morrison, D. (Ed.), *Satellites of Jupiter*. University of Arizona Press, Tucson, pp. 435–520.
- Smith, B.A., Voyager Imaging Team, 1979a. The Jupiter system through the eyes of Voyager 1. *Science* 204, 951–972.
- Smith, B.A., Voyager Imaging Team, 1979b. The Galilean satellites and Jupiter: Voyager 2 imaging science results. *Science* 206, 927–950.
- Squyres, S.W., 1980. Volume changes in Ganymede and Callisto and the origin of grooved terrain. *Geophysical Research Letters* 7, 593–596.
- Strom, R.G., Trask, N.J., Guest, J.E., 1975. Tectonism and volcanism on Mercury. *Journal of Geophysical Research* 80, 2478–2507.
- Taylor, J.R., 1996. *An Introduction to Error Analysis: the Study of Uncertainties in Physical Measurements*, 2nd ed. University Science Books, Herndon, Va. 327pp.
- Thomas, P.G., Allemand, P., 1993. Quantitative analysis of the extensional tectonics of Tharsis Bulge Mars: geodynamic implications. *Journal of Geophysical Research* 98, 13,097–13,108.
- Wernicke, B., Burchfiel, B.C., 1982. Modes of extensional tectonics. *Journal of Structural Geology* 4, 105–115.